International Journal of Heat and Mass Transfer 179 (2021) 121714

Contents lists available at ScienceDirect

International Journal of Heat and Mass Transfer

journal homepage: www.elsevier.com/locate/hmt

Enhanced wickability of bi-particle-size, sintered-particle wicks for high-heat flux two-phase cooling systems

Munonyedi Egbo, Jacob Keese, Gisuk Hwang*

Department of Mechanical Engineering, Wichita State University, Wichita, KS 67260 United States

ARTICLE INFO

Article history:
Received 25 March 2021
Revised 9 June 2021
Accepted 7 July 2021

Keywords:
Enhanced capillary flow
Permeability
Effective capillary meniscus radius
Capillary pumping limit

ABSTRACT

Two-phase thermal management systems such as heat pipes and vapor chambers offer high heat flux cooling performance in modern electronics and spacecrafts. However, the cooling performance is limited by poor wickability, i.e., ratio of permeability to capillary pumping capability, K/r_{eff}. In this study, we examine the enhanced wickability using bi-particle-size, sintered-particle wicks. The bi-particle-size wicks are sintered particle wicks having two different particle sizes (200/60, 200/100, 350/60, 550/60 μm) with two different particle weight ratios (75:25 and 50:50 wt%), and the wickability are characterized using a rate-of-rise method with FC-72 as a working fluid. It is found that the single-layer 200/100 μm (50:50 wt%) bi-particle-size wick enhances the wickability K/r_{eff} by 27% and 35%, compared to that of 200 and 60 μm uniform particle wick, respectively. This enhancement is due to the increased permeability from the large particle size and the reduced effective capillary meniscus radius from the small particles. This work provides an insight into advanced wick designs for high heat flux two-phase cooling systems.

1. Introduction

Two-phase thermal management systems, such as heat pipes (HPs) and vapor chambers (VCs), provide much larger heat flux cooling capability than that of single-phase cooling systems, by employing latent heat during liquid-vapor phase change process, i.e., phase-change heat transfer [1,2]. A wick is an essential component to supply liquid coolant to an evaporator, but the cooling performance is limited by the poor capillary flow near the evaporator. Common wick structures include wire meshes, grooves, fibers, and sintered particles, and comparative studies have identified sintered-particle wicks as the most effective structures for capillary flow and phase-change heat transfer characteristics. Several studies have shown that the capillary flow and phase-change heat transfer performance further increase with pore-scale composition [3–7]. The wick performance is often characterized by the wickability, i.e., ratio of the permeability to capillary pressure (or effective pore size), K/r_{eff}, and an optimal wick performance requires the maximum wickability. The wire meshes and groove wicks provide a large permeability with small capillary pumping capability, while fibers and thin sintered-particles are known for their characteristic large capillary pumping capacity and high resistance to liquid flow due to the large pressure drop resulted from the small characteristic pore sizes [8,9].

To enhance the wickability, i.e., simultaneously increasing permeability and capillary pumping capability, numerous approaches have been explored by combining the different characteristic microstructures, e.g., grooves with particles, and similar characteristic structures but different characteristic size, e.g., different particle sizes, i.e., composite wick. For the different characteristic micro structures, Deng et al. [2] have developed a composite wick by combining the V-grooves with the spherical/non-spherical particles, and characterized the permeability and other capillary flow properties such as porosity and maximum capillary pumping pressure, for two-phase heat transfer devices. To manufacture the copper composite wick, the micro-V-grooves with the size of 0.8 (H) × 0.45 (W) × 0.45 mm (P) have filled with the different copper particle sizes (<50, 50–75, 75–110 and 110–150 µm) and different particle shapes (spherical or irregular shape). Each composite wick has been sintered to have a thickness of 0.3 mm above the V-groove. The measured permeability has been much higher than those of the sintered particles because the micro grooves enhance the capillary flow. The composite wicks have also yielded larger capillary pumping capabilities than the V-groove in presence of the interconnected pore network provided by the sintered particles. Also, the composite wicks with irregular-shaped particles have had larger permeability than those with spherical particles, since the irregular-shaped particles have improved the pore networks for the capillary flow. Deng et al. [10] have also character-

* Corresponding author.
E-mail address: Gisuk.Hwang@wichita.edu (G. Hwang).

https://doi.org/10.1016/j.ijheatmasstransfer.2021.121714
0017-9310/

Nomenclature

c	lattice parameter, m
d	particle diameter, m
g	gravitational acceleration, m/s^2
h	height, m
K	permeability, m^2
l	length, m
m	mass, kg
$\dot{m}$	mass flow rate, kg/s
Δp	pressure drop, Pa
r	radius, m
t	time, s
v	velocity, m/s
V	volume, m^3

Greek symbols

ε	porosity
ρ	density, kg/m^3
σ	surface tension, N/m
θ	contact angle, degree
μ	dynamic viscosity, Pa-s

Subscripts

eq	equilibrium
eff	effective
l	liquid
p	particle
s	solid

ized the wickability of sintered particle wicks for "loop heat pipe" (LHP) application using the rate-of-rise test with an "infrared" IR thermal imaging. Two INCO Co. (Canada) – type 225 and 123 nickel wicks with particle size of 2.2 - 2.8 μm and 3 - 7 μm, respectively, and two spherical and irregular copper wicks of 75 – 110 μm with 95.5% purity which was supplied by Beijing Xinrongyuan Power Tech. Co. in China, have been characterized using ethanol and acetone as working fluids. They have reported that different working fluids have shown no significant difference in the experimental results. They have found that the permeability and wickability of the copper wicks outperformed those of the nickel wicks, and the type 255 nickel wick had superior permeability and wickability than the type 123, due to the larger porosity and smaller pores from the smaller particle size, which increase the permeability and capillary pumping pressure, respectively, in the former. Franchi and Huang [11] have developed a composite wick by sintering thin metal particles onto coarse copper meshes, aiming at enhancing the HP performance. The composite wick has significantly enhanced the phase-change heat transfer compared to wicks with uniform pore structures, concluding that the small pore in the thin layer of the sintered particles provided the capillary menisci for the capillary pumping, while the copper mesh served as the main fluid channels/passages. Oshman et al. [12] have also examined a composite wick by combining copper micro-pillars (100 μm high, 200 μm wide and 31 μm wide grooves) with a woven copper mesh (51 μm diameter wires with 76 μm spacing). They have found that the micro-pillar structures could only supply enough liquid to the evaporation sites at high power and high acceleration when they have been modified with woven copper mesh, concluding that the woven copper mesh offered larger capillary pumping by providing effective capillary menisci, while the micro-pillars provided wide channels for the liquid flow.

For the similar characteristic structures but different characteristic particle size wick, the cluster of the particles have been developed to simultaneously have the small characteristic pores (from the sintered particles) and the large pores (from the sintered clusters), so called bi-porous wick. The small pores promote capillary pumping, while the larger pores provide passages for large permeability. Note that previous studies focused on the single-phase flow characteristics through non-uniform particle size porous media such as permeability, boundary velocity, drag coefficient, and drag force for the fluidize bed reactors and sediments [13–15], while others focused on characterizing the two-phase cooling performance of bi-porous wicks [16–18]. Semenic and Catton [16] have studied the enhanced pool boiling performance with bi-porous wicks by comparing with mono-porous wicks. They have found that the best mono-porous wick (average particle diameter, $<d_p>$ = 107 μm, wick thickness = 500 μm) achieved a CHF of 300 W/cm^2 (21°C superheat), the best thin bi-porous wick ($<d_{p,1}>$ = 455 μm, $<d_{p,2}>$ = 63 μm, 800 μm) had approximately 73% higher CHF at 50 °C superheat, while the best thick bi-porous wick ($<d_{p,1}>$ = 455 μm, $<d_{p,2}>$ = 63 μm with the thickness of 3,000 μm) had a CHF value of 990 W/cm^2 (147°C superheat). They have concluded that the relatively high CHF in the thin bi-porous wicks is related to the active evaporating capillary menisci that exist throughout the entire wicks, i.e., both on top and within the wick surface, unlike in the mono-porous wicks with active evaporating capillary menisci present only on top of the entire wick. Semenic and Catton [16] also documented that thick bi-porous wicks were able to achieve even higher CHF values compared to the thin bi-porous wick because of the continued liquid supply by the upper parts of the wicking structure to the active evaporating menisci (thin film) above the center of the wick at high heat fluxes. Byon and Kim [17] have measured the enhanced wickability (K/r_{eff}) of bi-porous wicks, and developed a semi-analytic model to explain the enhanced capillary flow and optimize the bi-porous wicks, and it has predicted that the wickability of the former, 125/675 μm, was 11 times higher than that of the latter, 125 μm. The model has also showed that optimal wickability can be achieved when the ratio of the cluster size to the particle size is between 4 and 6. Also, Egbo et al. [18] have studied the phase change heat transfer characteristics of the bi-particle-size, thin sintered particles wicks in the upside down vapor chambers. The bi-particle-size wicks have been the sintered particle wicks with the different copper particle diameters, 60/200, and 100/200 μm with 1 to 3 particle layers, and the enhanced heat transfer performance was compared to the uniform particle size sintered particle wicks using 30, 60, 100, and 200 μm. It is found that the three-particle layers, bi-particle-size wicks, achieved the highest CHF values, 197 W/cm^2 (47.0 °C superheat) and 223 W/cm^2 (38.6°C superheat), for the 60/200 and 100/200 μm particles, respectively, relative to those of three-particle layers uniform particle wicks, 160 (31.7), 164 (33.4), 158 (38.8), and 175 W/cm^2 (36.0°C superheat) for the 30, 60, 100, and 200 μm particles, respectively. They have concluded that the performance of the bi-particle wicks results from the simultaneous increase in the capillary pumping capability and permeability offered by the smaller particles (smaller pore sizes) and the larger particles (larger pore sizes), respectively.

To further understand the enhanced capillary flow using the bi-particle-size wicks, this study examines the enhanced wickability of the thin sintered-particle wicks with bi-particle sizes using the rate-of-rise test. The enhanced wickability of the bi-particle-size wicks are compared to that of the thin sintered-particle wicks with uniform particle sizes.

2. Experimental

2.1. Sample fabrication

In this study, three different types of wicks were fabricated, (i) single-layer, uniform-particle size wick, (ii) single layer, bi-particle

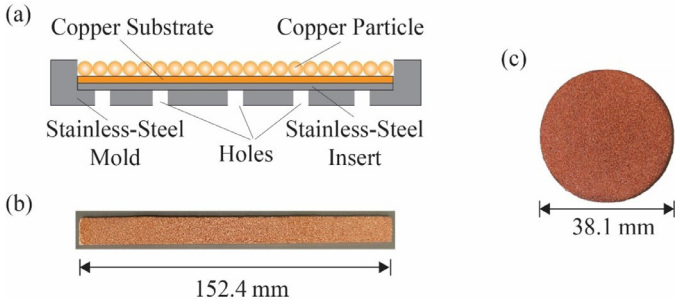

Fig. 1. (a) Schematic of fabricating sintered particle wick using designed stainless-steel mold. The copper particles, copper substrate, stainless-steel insert, and holes are also shown. The images of fabricated (b) thin rectangular wick used in the rate-of-rise test, and (c) thin circular wick used in the porosity measurement.

size wick, and (iii) multi-layer, uniform-particle size wick. Also, to measure the rate-of-rise and porosity, two different types of wicks were fabricated. For the rate-of-rise test, the wicks were furnace-sintered on thin rectangular copper stripe (12.7 mm-wide, 1.6 mm-thick, and 152.4 mm long), while for the porosity measurement, the wick sample were sintered on a circular copper substrate, 38.1 and 0.8 mm in diameter and thickness, respectively. The copper particles were purchased from CuLox, and those were used as received. The nominal copper particle sizes were 30, 60, 100, 200, 350, and 550 μm, with average mesh size of 400, 230, 140, 70, 45, and 35, respectively. The copper substrates were polished by sanding the surface using P400 grit, to remove surface structural defects such as small scratches and dents. Note that the circular wicks were manufactured using the same sintering process as found in our previous study [18], while the fabrication process for the rectangular wicks are found below. The image of the fabricated circular wick is shown in Fig. 1(c).

The technique used for preparing a test sample was dependent on the number of particle layers, as described below. The copper-particle-filled substrate was then inserted into an MTX OTF-1200X tube furnace for sintering. The tube furnace heated up the samples slowly, to a maximum temperature of 1000°C at which was held for 3 h [19]. Argon gas was passed through the tube, preventing from oxidation during the sintering process. Once the heating/cooling cycle was finished, the samples were removed and carefully demolded. The molds for the rectangular samples also had stainless-steel inserts [see Fig. 1(a)] that were placed below the substrates and could be pushed out along with the sample through holes drilled in the back of the mold as shown in Fig. 1(a) [19]. The image of the fabricated thin rectangular wick is shown in Fig. 1(b).

For the single layer sample with the large particle size, i.e., 200, 350, and 550 μm, a stainless steel mold was fabricated as shown in Fig. 1(a), which was similarly used in the previous study [19]. The polished copper substrate was placed into the stainless-steel mold with loose fit, and copper particles were then slowly poured onto the top of the substrate. The mold was tapped and rotated to ensure a single layer of the tightly packed particles was formed for the furnace sintering. For particle sizes below 200 μm, this approach was very difficult to form a single layer of the particles, and the following approach was developed as follows. The substrate was placed on a small ceramic tile and several drops of water were placed on the copper substrate until the water spread out to cover the surface (the water stayed only on the substrate because of the high contact angle with copper). Next, the particles were dropped onto the water, where they floated instead of sinking, because of the high surface tension of water and the small particle size. The particles would spread out on the surface of the water until they covered it completely with the single layer of particles. Then, the water was allowed to slowly evaporate for tightly packed particle arrangement.

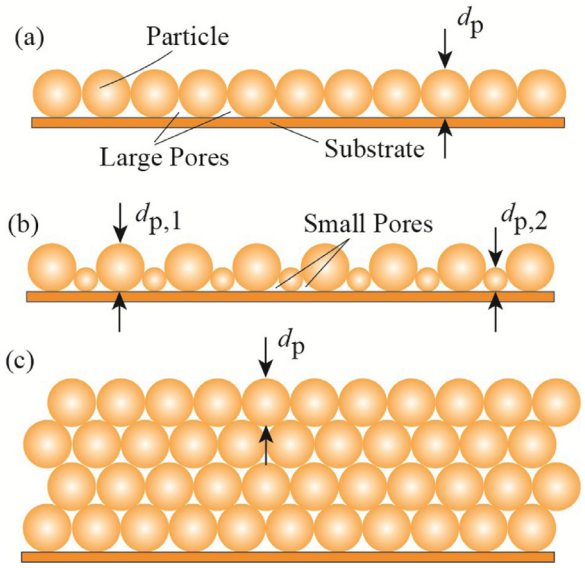

Fig. 2. Schematic of (a) single-layer uniform particle size wick with the uniform particle diameter d_p, (b) single-layer, bi-particle size wick with the larger particle diameter $d_{p,1}$ and smaller particle diameter $d_{p,2}$, and (c) multi-layer uniform particle size wick with the uniform particle diameter d_p. In (a) and (b), the large pores in the single-layer particle size wick and the small pores in the single-layer bi-particle wick are also shown.

The single-layer samples with the bi-particle size particles, i.e., 200/60, 200/100, 350/60, and 550/60 μm, were fabricated in two steps. First, a single layer of the loosely packed, larger size particles was prepared to ensure the large pores among the large particles, followed by the sintering. Then, the smaller particles were added to the sintered wick for the desired mass ratio of the large/small particles, followed by the second sintering. Schematics of the single-layer uniform particle size wick and single-layer bi-particle-size wick are shown in Fig. 2(a) and (b), respectively.

For the 100, 200, 350, and 550 μm multilayer samples, a substrate was placed into the stainless-steel mold and copper particles were added up to the top of the mold, allowing for the wick thickness of 4 to 5 particle layers. The sample was then sintered in the tube furnace as previously described. Schematic of a multi-layer uniform size particle wick is shown in Fig. 2(c).

The Scanning Electron Microscope (SEM) images of the characteristic particle distributions and pore structures of the single-layer wicks with 100, 200, and 200/100 μm particle sizes, and multi-layer wick with 100 μm particle size are shown in Fig. 3.

2.2. Porosity measurement

The porosity was measured based on the previous study [20], and the detailed measurement procedure is found in the previous work [19]. The measurement procedure is as follows: a dry wick sample, shown in Fig. 4(a), was placed on a digital mass balance (RADWAG; Model: AS 60/220.R2), and the balanced was tared. Acetone was then added via pipette until the wick was fully flooded, i.e., wick surface was covered by excessive acetone, as shown in Fig. 4(b). The liquid height reduces due to the evaporation, and it was visually monitored until the liquid level receded just below the top of the top particles of the wick as shown in Fig. 4(c).

Using the mass of pore-filled acetone, the porosity, ε, is determined using given relation as [20]

$$\varepsilon = \left[1 + \left(\frac{m_s}{\rho_s}\right)\left(\frac{\rho_l}{m_l}\right)\right]^{-1} \quad (1)$$

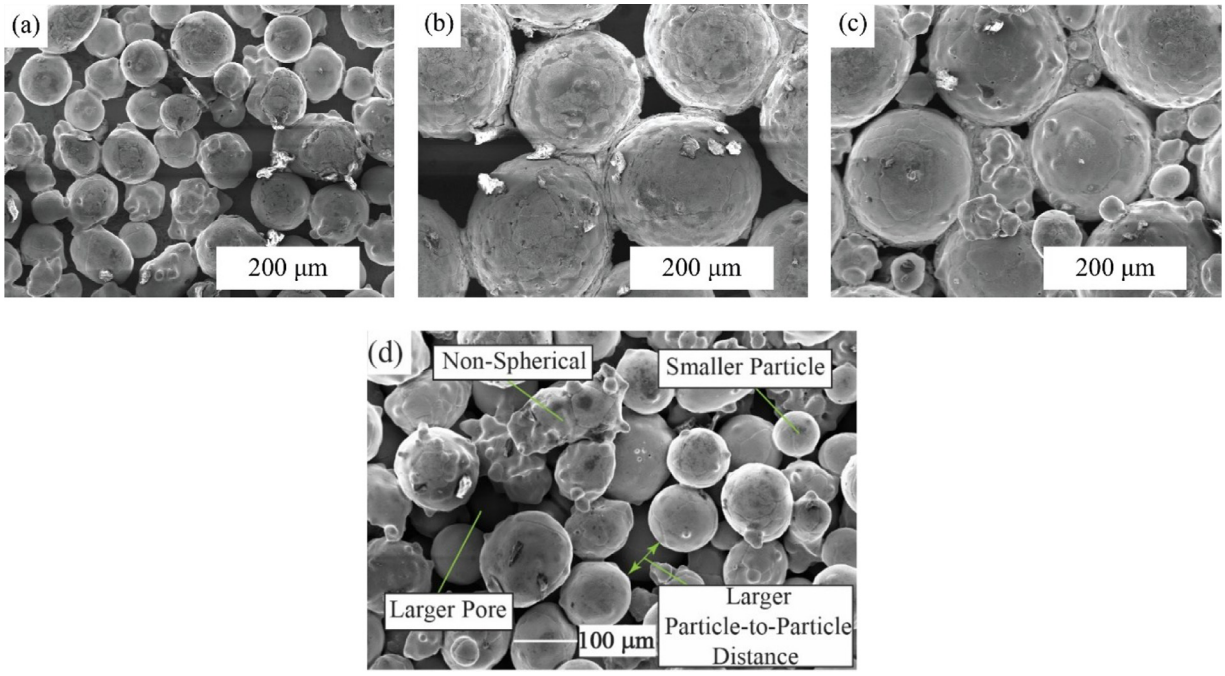

Fig. 3. SEM images of single-layer wicks with (a) 100 μm, (b) 200 μm, (c) 100/200 μm (50:50 wt%) particle sizes. (d) Multi-layer wick with 100 μm particle size (top view).

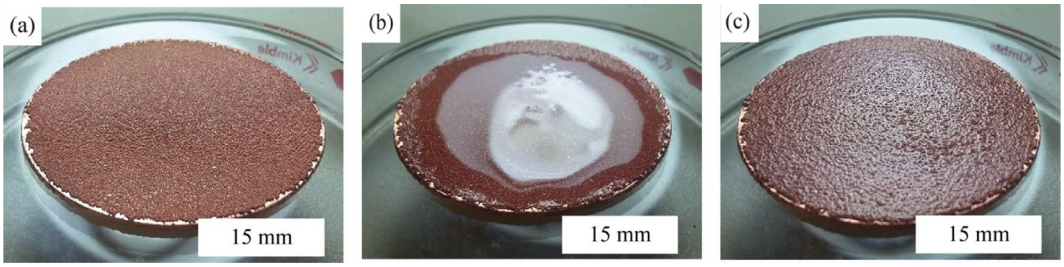

Fig. 4. Images during porosity measurement using acetone. (a) Dry wick, (b) flooded wick, and (c) saturated wick.

Table 1
Characteristic average particle diameter and particle-particle distance of single layer wick

Sample Description	Average Diameter, $<d_p>$ (μm)	Average Distance, l_p (μm)	Predicted Porosity, ε
Nominal particle diameter, 30 μm	26.9	31.4	0.56
60 μm	54.7	63.5	0.55
100 μm	79.4	89.2	0.52
200 μm	194.3	213.9	0.50
350 μm	332.2	391.3	0.52
550 μm	489.6	563.2	0.54

where m_s and m_l are the solid (copper) and liquid (acetone) mass, and ρ_s and ρ_l is the solid (copper) and liquid (acetone) density, respectively. The measured porosity was reported as an average value from five-time measurements, and those were compared with the predicted porosity from the microscopic image analysis. The samples were placed under an optical microscope with video recording capability. The magnification was set to 10 times, and images of the samples were observed on the computer. Using the program AmScope^{TM}, the computer-generated straight lines were drawn on the images between the centers of adjacent particles to measure the distance between them. A cumulative average distance between particles was calculated, and it reaches an asymptote within $\pm$ 2 μm, when the numbers of the particle-particle distance calculations were greater than 75. Then, additional 75 particle center-to-center distances were measured to report the average distance, as summarized in Table 1.

A similar image analysis was performed to quantify the average particle size for the single layer samples from the same optical microscope images. The computer-generated representative circles were drawn on the peripheral lines of the particles with the computer program such that the circles were concentric and equal in diameter with the particles, and then the diameter of the representative circles were calculated for the particle diameters. The 75 measurements were made, with the average value for each number of measurements being plotted. The average of the average diameter at each measurement after 35 measurements was then taken and is also reported in Table 1 for the 30, 60, 100, 200, 350, and 550 μm single layer samples.

The porosity was predicted using the calculated particle diameters and particle-particle distances under the assumption of the hexagonal unit cells as shown in Fig. 5. Then, the porosity is pre-

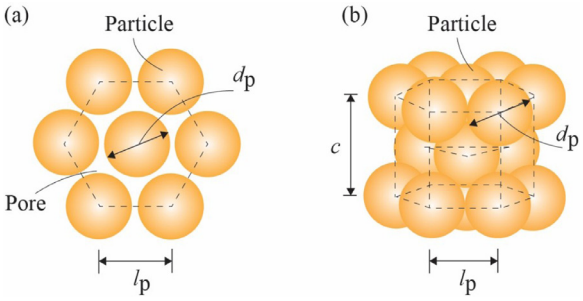

Fig. 5. Schematic of (a) a hexagonal particle arrangement of single-layer wick with the uniform particle size in the hexagonal unit cell, and (b) a hexagonal close-packed (HCP) particle arrangement of multi-layer with the uniform particle size. The particle diameter, d_p and particle-particle distance, l_p, lattice parameter, c, and pores are also shown.

dicted using the relation given as

$$\varepsilon = 1 - \frac{V_p}{V_t}, \tag{2}$$

where V_p and V_t are the particle volume and total volume in the hexagonal unit cell, respectively, which can be predicted as

$$V_t = \frac{3\sqrt{3}l_p^2 d_p}{2} \text{ and } V_p = \frac{\pi d_p^3}{2}, \tag{3}$$

where d_p is the particle diameter, and l_p is the particle-particle distance. Thus, we have

$$\varepsilon = 1 - \frac{\pi d_p^2}{3\sqrt{3}l_p^2} \tag{4}$$

To predict the porosities of the multi-layer unform particle wicks, we assume that the particles are closely packed in 'hexagonal close-packed' (HCP) unit cells as shown in Fig. 5(b). The 'atomic packing factor' (APF) of the HCP unit cell is calculated as $[(\pi <d_p>^3)/ (3\sqrt{2}l_p^3)]$. With the assumption that the particle-to-particle distance is the same as the particle diameter, the porosity ε is given as 1 – APF (= 1 – $[\pi/ (3\sqrt{2})]$). Note that from this expression the porosity of the multi-layer wick structure is independent of the particle size, and the value is approximately 0.26.

2.3. Permeability measurement: rate-of-rise test

To measure the permeability, a rate-of-rise method was used [20]. Schematic of the rate-of-rise test setup is shown in Fig. 6(a) and (b). The wick was vertically oriented and lowered until its bottom end touched the top surface of a working liquid. Note that FC-72 was chosen as a working fluid because of desired wetting property, density, and surface tension. The liquid then roses through the wick against gravity due to the capillary flow. The liquid wetting front height change was recorded using optical camera through the transparent glass tube, and the recorded images were post-processed to measure the liquid front height at given time, t. The recorded video of the rate-of-rise was split into frames using an open-source video editor, VirtualDub™, and the liquid front height at given time was measured using another open-source image processor ImageJ™. The rate-of-rise was then produced by plotting the measured heights of the rising liquid against their corresponding elapsed time. The snapshots of the liquid front rise with respect to time are shown in Fig. 7.

The measured liquid front height h as a function of time t was used to calculate the permeability K by curve fitting using the given relation [20]

$$h\frac{dh}{dt} = \frac{K}{\varepsilon\mu}\left(\frac{2\sigma}{r_{eff}} - \rho g h\right) \tag{5}$$

where σ, μ, and ρ is the surface tension, dynamic viscosity, and density, respectively, ε and r_{eff} are the porosity and effective capillary meniscus radius, and g is the gravitational acceleration.

The measured permeability of the uniform particle size wicks can be predicted using Kozeny-Carman relation given as [21]

$$K = \frac{\varepsilon^3 d_p^2}{a(1-\varepsilon)^2} \tag{6}$$

where a is the constant, ε is the porosity, and d_p is the particle diameter.

2.4. Effective capillary meniscus radius measurement

The effective capillary meniscus radius r_{eff} was characterized by measuring the equilibrium liquid height using given relation as

$$r_{eff} = \frac{2\sigma}{\rho g h_{eq}} \tag{7}$$

where σ is the surface tension, ρ is the density, g is the gravitation acceleration, and h_{eq} is the equilibrium liquid height. Note that the above relation is based on the perfect liquid wetting, i.e., contact angle of 0°. The equilibrium liquid height was measured when the liquid front height does not change with respect to time using the rate of rise test setup [Fig. 6(a) and (b)], and this measurement usually requires a minimum of 8 hours, depending on the characteristics of the wicks.

3. Results and discussion

3.1. Porosity

The measured (Eq.(1)) and predicted (Eq.(4)) porosities of the single- and multi-layer wicks with uniform and bi-particle size particles are summarized in Table 2. Note that the measured porosity ε is the average of five measurements for each wick, and the corresponding standard deviation of the porosity of each sample φ is also given.

The measured porosities of the single-layer uniform particle size wicks (Sample #1 - #5) are in the range of 0.47 to 0.64 with the minimal standard deviation $\varphi < 0.001$, while the predicted porosities using Eq.(4) are from 0.5 to 0.56. The maximum discrepancy between the measured and predicted porosities is 23%, and this is for Sample #3 (i.e., 100 μm wick). The discrepancies between the measured and predicted porosities are related to the particle arrangements, i.e., the predicted porosity (Eq.(4)) is based on the assumption that the particles are arranged in hexagonal unit cells (Fig. 5(a)), however, the SEM images of the manufactured wicks [see Fig. 3(a) and (b)] show that the unit cells are in fact are not organized to fit a defined unit cell arrangement. From Table 2, it is evident that the percentage discrepancy is more significant in particle sizes less than 200 μm (i.e., Sample #1 - #3). This may be attributed to the existence of loosely packed regions in the smaller-particle wick samples. Note that manufacturing single-layer wicks from smaller particle are more technically challenging with the manual particle arrangement used in this study. For Sample #4 (i.e., 200 μm) and #5 (i.e., 550 μm), the percentage difference is only 4 and 8%, respectively, because making tightly packed single-layer wicks using larger particle sizes is more effective and technically less challenging. Also, note that the measured porosities of the single-layer uniform particle size wicks are higher than those of the multi-layer uniform particle size wicks because the single layer particle arrangement has a larger pore space on the top of the layer, i.e., open space and possible loose particle packing in the fabrication process. However, the porosities of the bi-particle-size wicks, i.e., 200/60 (Samples #6 and 7) and 200/100

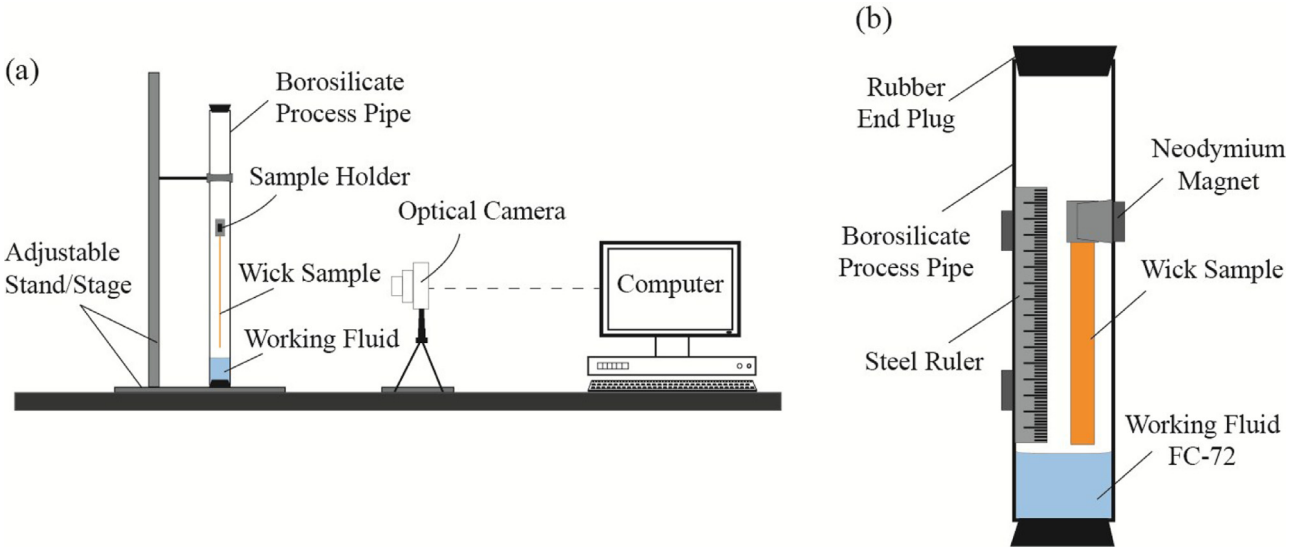

Fig. 6. Schematics of (a) rate-of-rise setup and (b) camera view of the wick, glass tube, ruler, and working fluid.

Table 2
Summary of the measured and predicted porosity, measured effective capillary meniscus radius, reciprocal of the effective capillary meniscus radius, and measured permeability for wick samples.

Sample #	Particle size, $<d_p>$, μm	Measured Porosity, $\varepsilon \pm \varphi$	Predicted Porosity, ε	Effective Capillary Meniscus Radius, r_{eff}, μm	$1/r_{eff}$, μm^{-1}	K, μm^2	K/r_{eff} (μm)
Single Layer							
1	30	0.48 ± 0.0022	0.56	10.8	0.0926	1.72	0.1588
2	60	0.59 ± 0.0022	0.55	13.8	0.0725	3.82	0.2767
3	100	0.64 ± 0.0022	0.52	15.4	0.0649	4.05	0.2631
4	200	0.52 ± 0.0054	0.50	35.2	0.0284	10.3	0.2926
5	550	0.50 ± 0.0008	0.54	114.8	0.0087	16.5	0.1437
6	200/60 (75:25 wt%)	0.50 ± 0.0027	-	15.0	0.0667	5.53	0.3683
7	200/60 (50:50 wt%)	0.55 ± 0.0024	-	15.9	0.0630	5.93	0.3727
8	200/100 (75:25 wt%)	0.47 ± 0.0020	-	21.0	0.0476	5.36	0.2550
9	200/100 (50:50 wt%)	0.55 ± 0.0021	-	21.6	0.0463	5.82	0.2693
10	350/60 (50:50 wt%)	0.50 ± 0.0007	-	13.1	0.0763	3.28	0.2502
11	550/60 (50:50 wt%)	0.50 ± 0.0008	-	13.6	0.0735	2.11	0.1548
Multi-Layer (4 – 5 Layers)							
12	100	0.42 ± 0.0007	0.26	16.7	0.0599	2.72	0.1626
13	200	0.43 ± 0.0008	0.26	33.5	0.0299	8.31	0.2482
14	350	0.50 ± 0.0007	0.26	71.9	0.0139	14.5	0.2017
15	550	0.50 ± 0.0008	0.26	83.4	0.0120	26.1	0.3124

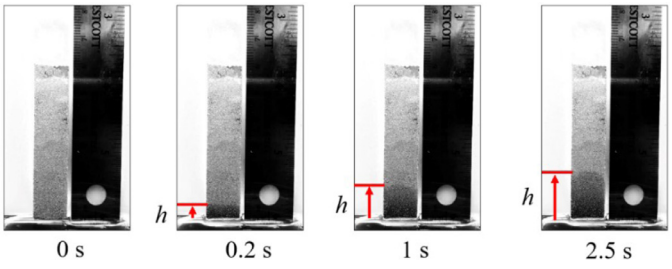

Fig. 7. Snapshots of rising liquid front in the wick at given elapsed time, t = 0, 0.2, 1, and 2.5 s. [19].

(Samples #8 and 9) show the smaller porosities than the uniform particle size wicks with 60, 100, and 200 μm (Samples #2, 3, 4) by reducing the pore space from the presence of interstitial particles, i.e., smaller particles, 60 and 100 μm fills in the pore space among the 200 μm particles. Similarly, the smaller porosity is found in 350/60 and 550/60 μm bi-particle wicks, compared to their corresponding uniform particle size wicks.

The multilayer, uniform particle 100 μm wick (Sample #12) has a porosity of 0.42, and the 200 μm wick (Sample #13) has a similar porosity of 0.43, which are smaller than their corresponding single-layer wicks. This smaller porosity may be related to the tightly packed particle arrangement between the layers, i.e., minimal pore space, in the multi-layer arrangement compared to the larger pore space between the single layer particles on substrate. In other words, the average distance between adjacent particles may be larger in single-layer particle arrangements than those in the multi-layer particle arrangements. Furthermore, the 350 and 550 μm wicks, i.e., Sample #14 and #15, respectively, has a porosity of 0.5 each, which are significantly larger than their corresponding predicted porosity of 0.26 for each. The same values of measured porosity agree with the assumption that the particles are in HCP unit cell arrangement in multi-layer wicks. This value, however, is significantly higher than the predicted porosity. The difference may be related to the particle size distributions and less-tightly-packed arrangements of each of the particle sizes wicks [see Fig. 3(d)] which could affect the average value of the lattice parameter c and the particle-to-particle distance l_p of the unit cells in the HCP particle arrangement shown in Fig. 5(b).

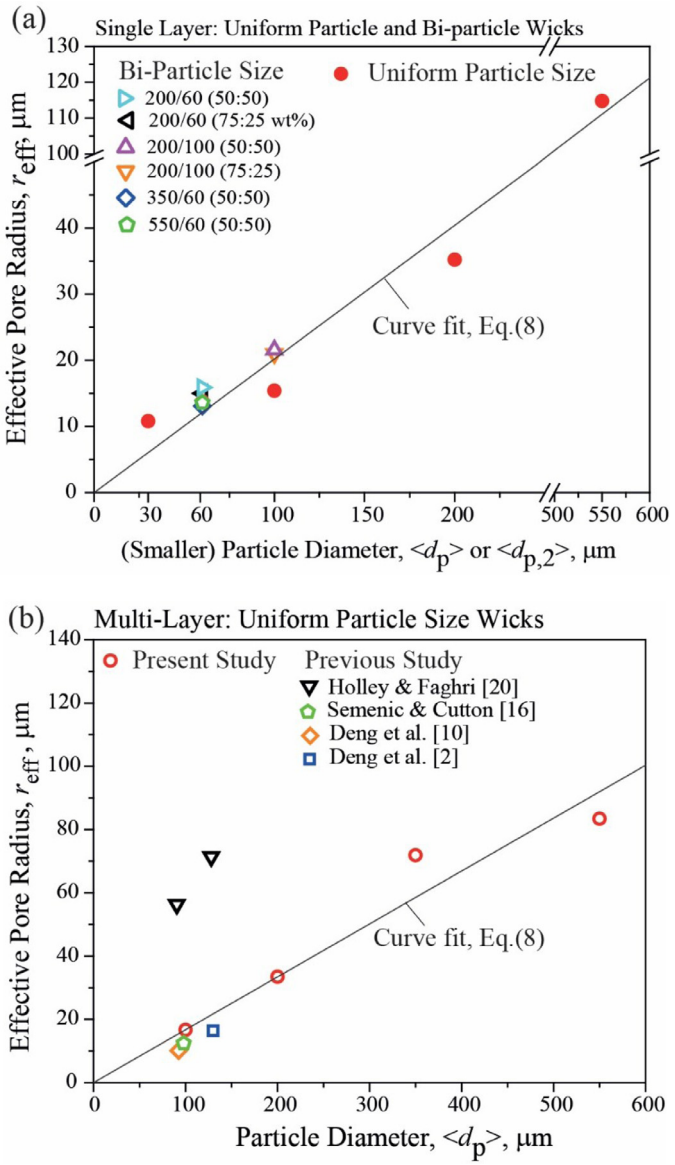

Fig. 8. Effective capillary meniscus radius, r_{eff} as a function of the particle diameter, $<d_p>$ for (a) single-layer, uniform- and bi-particle size wicks and (b) multi-layer, uniform particle size wicks. Fitted curves using based off the uniform particle size wicks are also shown. Note that the smaller particle size $<d_{p,2}>$ is used for the particle diameter, $<d_p>$ in (a) as it controls the capillary meniscus radius. Results of previous studies are also shown [2,10,16,20].

3.2. Effective capillary meniscus radius, r_{eff}

The measured effective capillary meniscus radius, r_{eff}, for the single-layer and multi-layer wicks as a function of the nominal particle diameter, $<d_p>$ is presented in Fig. 8(a) and (b), respectively. Note for the bi-particle-size wicks, the smaller particle diameter $<d_{p,2}>$ is used for the particle diameter $<d_p>$ as the data shows that they control the effective capillary meniscus radius. A summary of the effective capillary meniscus radius for the single- and multi-layer uniform particle size wicks and single-layer, bi-particle size wick is also found in Table 2. For the single-layer uniform- or bi-particle size wicks, Fig. 8(a) shows that the effective capillary meniscus radius increases almost linearly as the particle size (for uniform-particle size wick) or smaller particle size (for bi-particle size wick) increases, since the effective capillary meniscus radius increases with the characteristic particle diameter in sintered particle wicks. Note that the effective capillary meniscus radius of the bi-particle-size wicks does not significantly change with the particle size weight ratios, since they show the similar effective capillary meniscus radius between the 75:25 wt% and 50:50 wt% of 200/60 μm, and the 75:25 wt% and 50:50 wt% of 200/100 μm wicks. This indicates that even small presence of the smaller particle size controls the effective capillary meniscus radius. Similarly, Fig. 8(b) also shows that the measured effective capillary meniscus radius of the multi-layer uniform particle size wicks almost linearly increases with the particle diameter, and the results are compared to those in literature [2,10,16,20].

The measured effective capillary meniscus radius is well predicted as a function of the particle diameter, $<d_p>$, (for the uniform particle size wick) or a smaller particle diameter, $<d_{p,2}>$, (for the bi-particle size wick) using given relation as

$$r_{eff} = \alpha < d_p > \quad \text{or} \quad r_{eff} = \alpha < d_{p,2} >, \tag{8}$$

where α is the ratio between the effective capillary meniscus radius and characteristic particle diameter. The best curve fitted parameter is $\alpha = 0.202$ for the single-layer, uniform- and bi-particle size wick [Fig. 8(a)] or $\alpha = 0.2$ for the multi-layer uniform particle size wick [Fig. 8(b)], which are very similar to $\alpha = 0.205$ reported in the previous work [22].

The present exprimental results agree reasonably with those studied in Deng et al. [2,10], and Semenic and Catton [16], whereas they show smaller values than those measured in Holley and Faghri [20], for the multi-layer uniform particle wicks.

3.3. Permeability

Fig. 9(a) shows the measured rate-of-rise, i.e., liquid front height, h, as a function of time, t, of the single-layer, uniform particle size, 60 μm (Sample #2) and 200 μm (Sample #4), and bi-particle size 200/60 μm, 50:50 wt% (Sample #7) until the liquid front reaches the equilibrium height. At the early liquid front rising stage, i.e., $t < 10$ s, the liquid front increases rapidly, but it increases slowly as the elapsed time increases, i.e., $t > 10$ s. The small increase of the liquid front at $t > 10$ s is related to the fact that the hydrostatic pressure becomes larger as the liquid front height increases. At $t < 10$ s, the rate of rise for the single layer uniform particle size wick, 60 μm is smaller than that of 200 μm wick due to the smaller permeability, i.e., smaller particle size. However, at $t > 10$ s, the 60 μm equilibrated liquid front height is larger than that of 200 μm wick due to the smaller effective capillary meniscus radius, i.e., smaller particle size. However, the bi-particle size wick, e.g., 200/60 μm, 50:50 wt% takes advantage of the smaller effective capillary meniscus radius from the smaller particles, e.g., 60 μm and the larger permeability from the larger particles, e.g., 200 μm, showing the similar rate of rise to that of 200 μm wick at $t < 10$ s and similar maximum liquid front height to that of 60 μm wick at $t > 10$ s. The equilibrium height is attained by the force balance between capillary pressure and hydrostatic pressure. The measured equilibrium heights of the 60, 200, and 200/60 μm, 50:50 wt%, are 87.4, 29.2, and 76.2 mm, respectively. The smaller particle size wick, 60 μm, results in the larger equilibrium height than that of the larger particle size due to the smaller effective capillary meniscus radius formed between the smaller particles. On the other hand, the 200/60 μm, 50:50 wt%, bi-particle wick achieved equilibrium height comparable to that of the 60 μm uniform particle wick because of their comparable effective capillary meniscus radius, which controls the equilibrium height.

Fig. 9(b) shows the measured rate-of-rise as a function of time for the single-layer, uniform particle size, 60 μm (Sample #2) and 200 μm (Sample #4), and bi-particle size 200/60 μm, 50:50 wt% (Sample #7) at $t < 5$ s, which are used for curve fitting using

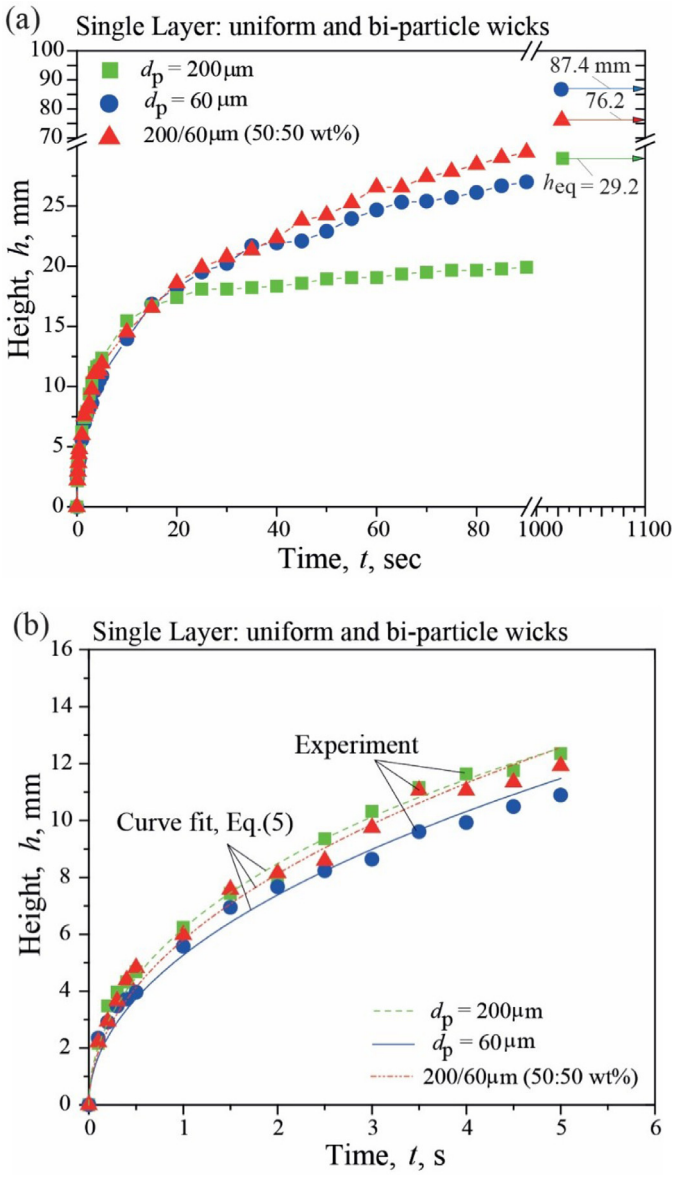

Fig. 9. (a) Rate of rise for single-layer, uniform 60 μm (Sample #2) and 200 μm (Sample #4), and bi-particle 200/60 μm, 50:50 wt% (Sample #7) size wicks. The equilibrium heights are also shown. (b) Liquid front height h, with respect to time at t < 5 s for the uniform (60 and 200 μm), and bi-particle [200/60 μm (50:50 wt%)] size wicks. The curve fit using Eq. (5) are also shown.

Eq. (5) via least squares method. The thermophysical properties of the working fluid (FC-72), the measured porosity (Section 2.2) and effective capillary meniscus radius (Section 2.4) of each wick are used in Eq. (5). Note that the permeabilities for other wicks are also calculated by curve fitting into the measured rate of rise [not shown in Fig. 9(a) and (b)], and the resulting permeabilities are found in Table 2.

Fig. 10(a) shows the measured permeabilities of single- and multi-layer uniform particle size wicks with respect to the particle diameter. The permeabilities of the single- and multi-layer uniform particle wicks increase exponentially as the particle diameter increases. Using the Kozeny-Carman relation (Eq.(6)) with measured porosity (Table 2), the best curve-fitted constant a is 2000 and 2900 for the single- and multi-layer wicks, respectively. Note that the constants are significantly higher than a = 180 for closely packed particle bed, i.e., the permeability is much lower than that of the closely-packed particle bed, and this is related to the fact that the pore connectivity of the thin wicks is substantially lower

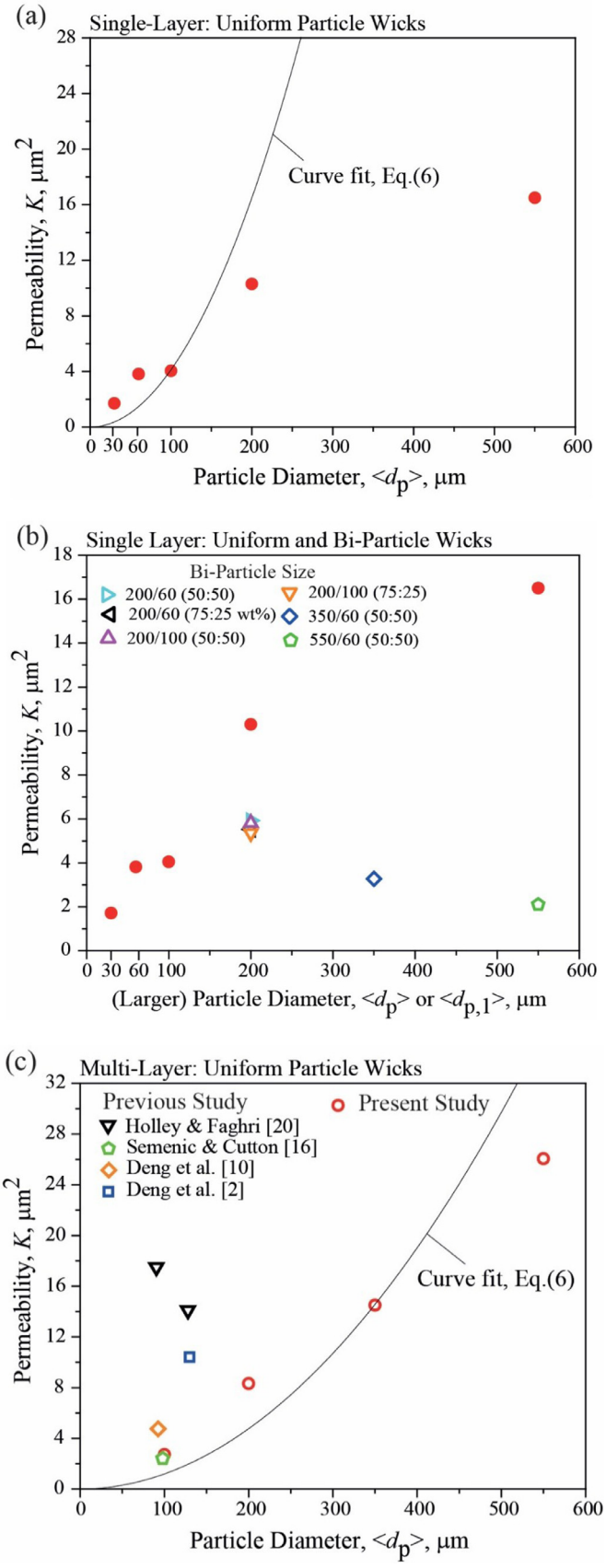

Fig. 10. Measured permeability as a function of the particle diameter for (a) single-layer, uniform particle size wicks including Kozeny-Carman relation, Eq. (6), and (b) single layer, uniform, and bi-particle size wicks. Note that the particle diameter for the bi-particle size wick is the larger particle diameter. (c) Multi-layer, uniform particle size wicks. The curve-fit is based off the uniform particle size wicks. The results from previous studies are also shown [2,10,16,20].

(due to 2D pore network) compared to that of the closely-packed particle bed (3D pore network). It is also noted that the presence of the substrate reduces the permeability due to the smaller pore size near the substrate compared to the large pores through the closely-packed particle bed without substrate. Note that the measured permeability of the 550 μm single-layer particle size wick is significantly lower than expected. This is considered an outlier, and this may be related to the existing large particle-to-particle distance which results in large effective capillary meniscus radius and consequently low capillary pumping through the wick.

Fig. 10(b) shows the permeability of the single-layer bi-particle size wicks as a function of the larger particle size, $d_{p,1}$, compared to that of the single-layer, uniform particle size wicks. The permeability of the single-layer, bi-particle size wick results in the smaller permeability than the permeability of the larger uniform particle size wicks, but larger than the permeability of the smaller uniform particle size wicks. This is because the smaller particles occupy the interstitial pore space between the larger particles, decreasing flow path through the inter-connected large pore network and reducing the pore size [see Fig. 3(c)]. For example, the permeability of the 200/60 μm, (50:50 wt%, Sample #7) bi-particle size wick is 5.93 μm^2, which is smaller than the permeability of the 200 μm uniform particle size wick (Sample #4), K = 10.3 μm^2, but larger than that of the 60 μm uniform particle size wick (Sample #2), K = 3.82 μm^2. The reduction of the permeabilities of the bi-particle size wicks become more pronounced at larger particle size difference. For example, the 200 μm uniform particle size wick (Sample #4) and the 200/100 μm (75:25 wt%, Sample #8) bi-particle size wick has a permeability of 10.3 and 5.36 μm^2, respectively, which is 48% difference. Furthermore, the permeability of the 550 μm (Sample #5) uniform particle wick, which is 16.5 μm^2, is 87% larger than that of the 550/60 μm, (50:50 wt%, Sample #11) bi-particle wick, which is 2.11 μm^2. Note that Fig. 10(b) also shows that the particle weight ratios such as 50:50 and 75:25 wt% have no significant effects on the permeability of the bi-particle wicks. For example, the 200/60 μm (50:50 wt%, Sample #7) and 200/60 μm (75:25 wt%, Sample #6) bi-particle wicks have similar permeability, 5.926 and 5.526 μm^2, respectively, i.e., only 7.2% difference. Similarly, the 200/100 μm (50:50 wt%, Sample #9) and 200/100 μm (75:25 wt%, Sample #8) bi-particle wicks have similar permeability, 5.817 and 5.355 μm^2, respectively, i.e., 8.6% difference.

Fig. 10(c) shows the current measured permeabilities of the multi-layer uniform particle wicks. It is evident that the permeability exponentially increases as the particle size increases, and this is attributed to that fact that the pore sizes, i.e., cross-sectional area of interconnected pores, as the particle size increases. These permeability data is curve-fitted with Kozeny-Carman relation (Eq.(6)), with the best curve-fitted constant a = 2,900. The constant a is significantly higher than a = 180 for closely packed particle bed, i.e., the permeability is much lower than that of the closely-packed particle bed, and this may be related to the particle size distribution and the particle arrangement. The current permeability data reasonably agree to the previous studies including Deng et al. [10], Semenic and Catton [16], but there are deviated from the results by Holley and Faghri [20] and Deng et al. [2] as shown in Fig. 10(c). The reason for this deviation may be related to the different nature of wicks (wicks without substrate and/or different sample thickness), testing method (pressure gradient method), fabrication technique (different sintering temperature/time), particle size distribution, etc.

3.4. Wickability vs capillary pumping capability

Fig. 11(a) and (b) shows the wickability, i.e., K/r_{eff}, as a function of the reciprocal of the effective capillary meniscus radius

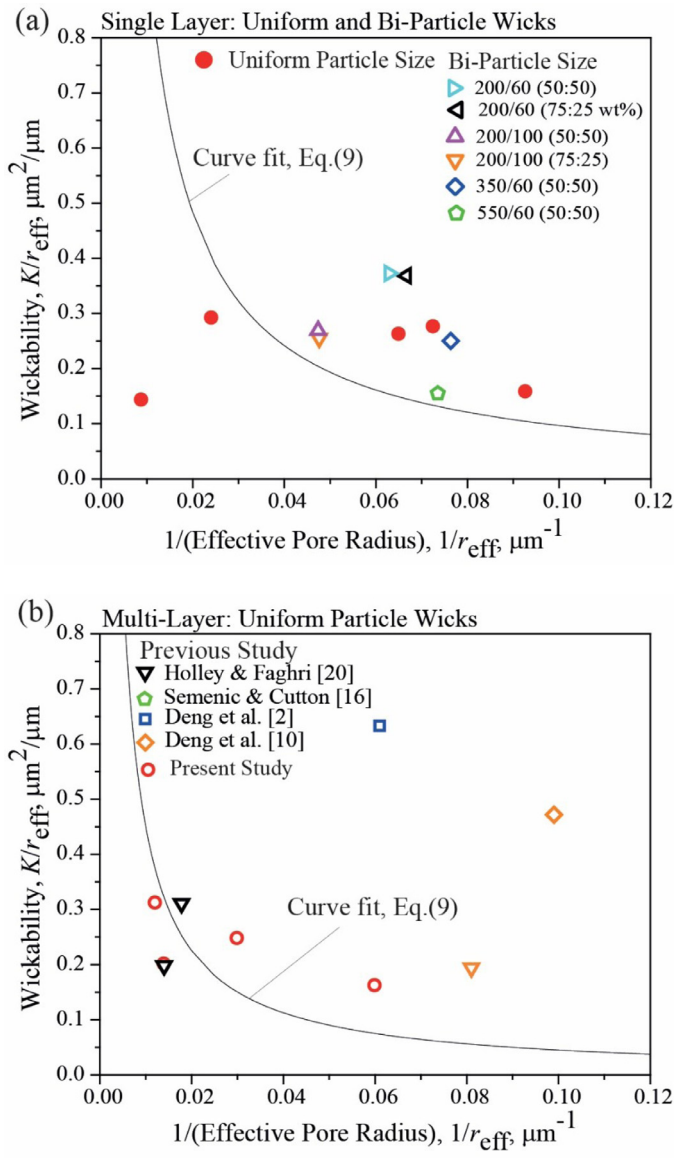

Fig. 11. Wickability as a function of the reciprocal of the effective capillary meniscus radius for (a) single-layer, uniform- and bi-particle wicks and (b) multi-layer, uniform-particle wicks. The modified Kozeny-Carman relation (Eq. (9)) is also shown. Previous results are also shown [2,10,16,20]. Note that the modified Kozeny-Carman relation is used to curve-fit the data for the single- and multi-layer uniform particle size wicks only.

$1/r_{eff}$ for the single-layer, uniform- and bi-particle size wicks and multi-layer, uniform particle size wicks to identify the desired wick structures having both the large K/r_{eff} and $1/r_{eff}$. Note that the desired wick structures needs both large wickability, i.e., K/r_{eff}, and capillary pumping capability, i.e., $1/r_{eff}$. In Fig. 11(a), the smallest uniform particle size wick, i.e., 30 μm (Sample #1) shows the best capillary pumping capability from the small effective capillary meniscus radius, i.e., $1/r_{eff}$ = 0.093 μm^{-1}, due to the small characteristic pore size, but the poor wickability, i.e., K/r_{eff} = 0.159 μm, due to the small permeability from the small pore size. As the particle size increases, the wickability increases from the large permeability, and the capillary pumping capability also decreases. The wickability of the 60 (Sample #2), 100 (Sample #3), and 200 μm (Sample #4) single-layer uniform wicks are 0.2767, 0.2631, and 0.2926 μm, respectively. The capillary pumping capability and wickability of the 550 μm single-layer uniform wick is the smallest because of its characteristic large pore sizes and thus large ef-

fective capillary meniscus radius, i.e., 114.8 μm. Although these large pore sizes offer large permeability, they result in poor capillary pumping capability. The predicted wickability with respect to the reciprocal of the effective capillary meniscus radius is shown in Fig. 11(a), using the modified Kozeny-Carman relation with the effective capillary meniscus radius and the average measured porosity of the uniform particle size wick (Table 2) given as

$$\frac{K}{r_{\text{eff}}} = \frac{\langle\varepsilon\rangle^3 r_{\text{eff}}}{a(1-\langle\varepsilon\rangle)^2} \tag{9}$$

Note that the Kozeny-Carman relation, Eq. (6) is a function of the particle radius, r_p, but here we use the effective capillary meniscus radius, r_{eff} using Eq. (8).

The relation shows that wickability decreases as the capillary pumping capability increases, and thus agrees reasonably with the experimental results.

For the bi-particle size wicks, it is found that the 200/60 μm (50:50 wt%, Sample #7) and 200/60 μm (75:25 wt%, Sample #6) have the largest wickability of 0.373 and 0.368 μm, with the reasonably good capillary pumping capability from the effective capillary meniscus radius of 15.9 and 15 μm, respectively. The large wickability is related to the combinations of the reduced capillary flow resistance from the inter-connected large pore network, i.e., 200 μm, and the large capillary pumping capability from the small pores, i.e., 60 μm. The 200/100 μm (50:50 wt%, Sample #9) and 200/100 μm (75:25 wt%, Sample #8) wicks show the similar wickability, i.e., 0.269 and 0.255 μm, and the effective capillary meniscus radius, i.e., 21.6 and 21 μm, respectively. These results indicate that the wickability and effective capillary meniscus radius are not strongly dependent on the particle weight ratio, but significantly dependent on the smaller particle size in bi-particle wicks. The bi-particle wicks manufactured from the combination of 60, 100, and 200 μm particle sizes enhance the wickability and effective capillary meniscus radius compared to the uniform-particle-size wicks from 60, 100, and 200 μm, and the wickability of the bi-particle-size wicks is higher than those of uniform particle wicks by at least 27%. For instance, the wickability enhancement is approximately 35% between the 60 μm and 200/60 μm (50:50 wt%) wicks.

Furthermore, the 350/60 μm (50:50 wt%, Sample #10) and 550/60 μm (50:50 wt%, Sample #11) single-layer, bi-particle wicks also result in the similar effective capillary meniscus radius to that of their smaller particle size uniform wick, i.e., 60 μm, however, the wickability is smaller than expected. The small wickability could be related to the particle size difference or due to the limitation of the present fabrication technique. Further study is needed to understand the exact origin of small wickability.

The wickability of multi-layer uniform particle wick of the present study is presented in Fig. 11(b), showing that the wickability and effective capillary meniscus radius decrease with the particle size, which is expected based on the Kozeny-Carman relation (Eq.(6)).

The results of the present study reasonably agree to those of Holley and Faghri [20], Semenic and Catton [16], and Byon and Kim [17], but significantly different from those of Deng et al. [2,10], for the multi-layer uniform particle wicks. Note that Deng et al. [2] studied the performance characteristics of composite wicks – grooved and sintered particles, which are known to have higher hydraulic and wickability. Thus, the reason for the higher wickability may be related to the higher permeability provided by the large capillary flow channel from the V-grooves.

4. Conclusion

The enhanced wickability K/r_{eff} of the bi-particle wicks are experimentally studied by characterizing the permeability K, and effective capillary meniscus radius r_{eff} using the rate-of-rise test. The bi-particle wicks are the single-layer, sintered copper particles of 200/60, 200/100, 350/60, 550/60 μm with the weight ratios of 50:50 wt% and 75:25 wt%. The wickability of the bi-particle wicks are compared with the single- and multi-layer uniform particle wicks, i.e., sintered-copper particles of 30 - 550 μm. The major findings from this study are summarized as follows:

1. The single-layer 200/100 μm (50:50 wt%) bi-particle wick enhances the wickability K/r_{eff} by up to 27 – 35%, compared to those of 200 and 60 μm uniform particle wick, respectively, mainly due to the smaller effective capillary meniscus radius associated with the smaller particle sizes and the larger permeability K associated with the larger particle sizes.
2. For the single-layer, bi-particle wicks, the effective capillary meniscus radius r_{eff} is controlled by the small particle size.
3. For the single- and multi-layer, uniform-particle size wicks, the effective capillary meniscus radius r_{eff} linearly increase with the particle size increases.

The obtained experimental work provides deep insights into the desired wick structure, enhancing both the wickability and capillary pumping capability using sintered particles with bi-particle size distributions for high heat flux, two-phase thermal management systems.

Declaration of Competing Interest

The authors declare that they have no known competing financial interests or personal relationships that could have appeared to influence the work reported in this paper.

CRediT authorship contribution statement

Munonyedi Egbo: Methodology, Investigation, Software, Writing – original draft. **Jacob Keese:** Methodology, Investigation, Software, Writing – original draft. **Gisuk Hwang:** Conceptualization, Supervision, Funding acquisition, Writing – review & editing.

Acknowledgement

This work is financially supported by NASA Cooperative Agreement Notice, Grant Number 80NSSC18M0030, National Science Foundation (NSF), Award No. OIA-1929187, and College of Engineering, Department of Mechanical Engineering, Wichita State University. The authors would like to thank Mr. Nathan Albu and Dr. Yahya Nasersharifi for their help in designing the mold and developing the wick manufacturing process, respectively. Authors would like to thank Dr. Massoud Kaviany at Department of Mechanical Engineering, University of Michigan, for thoughtful comments on the bi-particle size wick designs. Also, thanks to Dr. Mohammad Hassan (GRC) and Mr. Eric Sunada (JPL) for their helpful comments and advice. Thanks to Ms. Moriah Ausherman at Department of Mechanical Engineering, Wichita State University, Dr. Michael Sealy, Mr. Guru Charan Reddy Madireddy at the University of Nebraska-Lincoln, for the SEM images.

Reference

[1] Y. Tang, D. Deng, L. Lu, M. Pan, Q. Wang, Experimental investigation on capillary force of composite wick structure by IR thermal imaging camera, Exp. Therm. Fluid Sci. 34 (2) (2010) 190–196.
[2] D. Deng, Y. Tang, G. Huang, L. Lu, D. Yuan, Characterization of capillary performance of composite wicks for two-phase heat transfer devices, Int. J. Heat Mass Transf. 56 (1–2) (2013) 283–293.
[3] R. Ranjan, J.Y. Murthy, S.V. Garimella, Analysis of the wicking and thin-film evaporation characteristics of microstructures, J. Heat Transf. 131 (10) (2009) 101001.

[4] T.H. Bauer, A general analytical approach toward the thermal conductivity of porous media, Int. J. Heat Mass Transf. 36 (17) (1993) 4181–4191.
[5] A.A. El-Nasr, S.M. El-Haggar, Effective thermal conductivity of heat pipes, Heat Mass Transf. 32 (1–2) (1996) 97–101.
[6] M.G. Mwaba, X. Huang, J. Gu, Influence of wick characteristics on heat pipe performance, Int. J. Energy Res. 30 (7) (2006) 489–499.
[7] A. Gupta, G. Upadhya, Optimization of heat pipe wick structures for low wattage electronics cooling applications, in: Pacific RIM/ASME International Intersociety Electronics Photonic Packaging Conference, 26, 1999, pp. 2129–2137.
[8] W. Ling, W. Zhou, W. Yu, R. Liu, K.S. Hui, Thermal performance of loop heat pipes with smooth and rough porous copper fiber sintered sheets, Energy Convers. Manag. 153 (2017) 323–334.
[9] G. Kumaresan, S. Venkatachalapathy, L.G. Asirvatham, S. Wongwises, Comparative study on heat transfer characteristics of sintered and mesh wick heat pipes using CuO nanofluids, Int. Commun. Heat Mass Transf. 57 (2014) 208–215.
[10] D. Deng, D. Liang, Y. Tang, J. Peng, X. Han, M. Pan, Evaluation of capillary performance of sintered porous wicks for loop heat pipe, Exp. Therm. Fluid Sci. 50 (2013) 1–9.
[11] G. Franchi, X. Huang, Development of composite wicks for heat pipe performance enhancement, Heat Transf. Eng. 29 (10) (2008) 873–884.
[12] C. Oshman, et al., Thermal performance of a flat polymer heat pipe heat spreader under high acceleration, J. Micromechanics Microengineering 22 (4) (2012) 045018.
[13] F. Dorai, C.M. Teixeira, M. Rolland, E. Climent, M. Marcoux, A. Wachs, Fully resolved simulations of the flow through a packed bed of cylinders: effect of size distribution, Chem. Eng. Sci. 129 (2015) 180–192.
[14] M.A. van der Hoef, R. Beetstra, J.A.M. Kuipers, Lattice-Boltzmann simulations of low-Reynolds-number flow past mono-and bidisperse arrays of spheres: results for the permeability and drag force, J. Fluid Mech. 528 (2005) 233.
[15] V.S. Patwardhan, C. Tien, Sedimentation and liquid fluidization of solid particles of different sizes and densities, Chem. Eng. Sci. 40 (7) (1985) 1051–1060.
[16] T. Semenic, I. Catton, Experimental study of biporous wicks for high heat flux applications, Int. J. Heat Mass Transf. 52 (21–22) (2009) 5113–5121.
[17] C. Byon, S.J. Kim, Capillary performance of bi-porous sintered metal wicks, Int. J. Heat Mass Transf. 55 (15–16) (2012) 4096–4103.
[18] M. Egbo, Y. Nasersharifi, G. Hwang, Phase-change heat transfer of sintered–particle wick in downward facing orientation: particle size and wick thickness effects, Int. J. Heat Mass Transf. 155 (2020) 119840.
[19] N. Albu, J. Keese, G. Hwang, Bimodal, thin wick structures for high heat flux two- phase thermal control systems, Presented at the International Conference on Environmental Systems, Jul. 2019.
[20] B. Holley, A. Faghri, Permeability and effective pore radius measurements for heat pipe and fuel cell applications, Appl. Therm. Eng. 26 (4) (2006) 448–462.
[21] M. Kaviany, Principles of Heat Transfer in Porous Media, Springer Science & Business Media, 2012.
[22] G.P. Peterson, An Introduction to Heat Pipes: Modeling, Testing, And Applications, Wiley, New York, 1994.